

1 OBS noise reduction from horizontal and vertical
2 components using harmonic-percussive separation
3 algorithms

Zahra Zali^{1,2}, Theresa Rein¹, Frank Krüger¹, Matthias Ohrnberger¹, Frank Scherbaum¹

¹University of Potsdam, Institute of Geosciences, Karl-Liebknecht-Str. 24-25, 14476 Potsdam, Germany

²GFZ German Research Centre for Geosciences, Potsdam, Germany

Correspondence to: Zahra Zali (zali@uni-potsdam.de)

Zahra Zali: Campus Golm, Building 29, Room 2.48, Karl-Liebknecht-Str. 24-25, 14476 Potsdam, Germany
(zali@uni-potsdam.de)

Theresa Rein: Campus Golm, Building 27, Room 0.43, Karl-Liebknecht-Str. 24-25, 14476 Potsdam,
Germany (theresa.rein@uni-potsdam.de)

Frank Krüger: Campus Golm, Building 27, Room 1.36, Karl-Liebknecht-Str. 24-25, 14476 Potsdam,
Germany (Frank.Krueger@geo.uni-potsdam.de)

Matthias Ohrnberger: Campus Golm, Building 27, Room 1.37, Karl-Liebknecht-Str. 24-25, 14476
Potsdam, Germany (Matthias.Ohrnberger@geo.uni-potsdam.de)

Frank Scherbaum: Campus Golm, Building 29, Room 1.52, Karl-Liebknecht-Str. 24-25, 14476 Potsdam,
Germany (Frank.Scherbaum@geo.uni-potsdam.de)

Abstract

Records from ocean bottom seismometers (OBS) are highly contaminated by noise, which is much stronger compared to data from most land stations, especially on the horizontal components. As a consequence, the high energy of the oceanic noise at frequencies below 1 Hz considerably complicates the analysis of the teleseismic earthquake signals recorded by OBSs.

Previous studies suggested different approaches to remove low-frequency noises from OBS recordings, but mainly focused on the vertical component. The records of horizontal components, crucial for the application of many methods in passive seismological analysis of body and surface waves, could not be much improved in the teleseismic frequency band. Here we introduce a noise reduction method, which is derived from the harmonic-percussive separation algorithms used in Zali et al., (2021) in order to separate long-lasting narrowband signals from broadband transients in the OBS signal. This leads to significant noise reduction of OBS records on both the vertical and horizontal components and increases the earthquake signal-to-noise ratio (SNR) without distortion of the broadband earthquake waveforms. This is demonstrated through tests with synthetic data. Both SNR and cross-correlation coefficients showed significant improvements for different realistic noise realizations. The application of denoised signals in surface wave analysis and receiver functions is discussed through tests with synthetic and real data.

1 Introduction

Ocean bottom seismometer recordings are generally difficult to analyze, because the noise level is usually much higher compared to land stations. At frequencies below 1 Hz, the effect of the ocean noise, often dominates the data and hinders the seismological analysis (e.g. Webb et al., 1991; Crawford, 1994). Signals of interest, i.e. transient signals, especially from teleseismic events can be masked by the oceanic noise. Here, the horizontal components are most strongly contaminated by low frequency noise. To illustrate the noise on OBS data, we exemplarily show the records of the station D10 of the DOCTAR array (see Fig. 1 and Fig. S1). Various studies tried to identify and characterize the different sources of noise recorded at the ocean bottom (e.g. Webb, 1998; Crawford & Webb, 2000; Corela, 2014; Stähler et al., 2018; Essing et al., 2021; An et al., 2021). In our study, we focus on noise sources that especially affect teleseismic horizontal recordings in the frequency band of 0.02–2 Hz. Generally, the dominant natural noise signals in the oceanic environment are secondary oceanic microseisms (Rayleigh/Scholte waves at the ocean bottom) caused by the interaction of wind-generated water waves, infragravity waves (compliance noise) as well as tilt noise; the latter originates from the turbulent interaction between currents and the instrument (e.g. Crawford et al., 1998; Corela, 2014). Primary oceanic microseism, originates from the interaction of water waves incident at steep coastlines and/or rough seafloor (Hasselmann, 1963; Webb, 1998; Bell et al., 2015). Its spectral peak is around 0.07 Hz (Friedrich et al. 1998) in the Northern Atlantic. The secondary microseism has frequencies above 0.1–0.25 Hz, with a highest spectral peak around 0.14 Hz (Friedrich et al., 1998, Fig. 1). It is caused by wind or swell waves propagating in opposite directions. The primary and secondary microseisms affect both the vertical and horizontal seismometer components, whereas the compliance noise

Zahra Zali 10.1.2023 19:59

Deleted: is

Zahra Zali 10.1.2023 19:59

Deleted: ing

Zahra Zali 10.1.2023 20:00

Deleted: is

Zahra Zali 10.1.2023 20:01

Deleted: ing

Zahra Zali 10.1.2023 20:02

Deleted: is

Zahra Zali 10.1.2023 20:02

Deleted: ing

63 is solely observed on the vertical component and the hydrophone. Compliance noise, dominant in the
 64 frequency band of 0.01–0.04 Hz, is only significant if its wavelength exceeds the water depth (Crawford et
 65 al., 1998; Crawford & Webb, 2000; Bell et al., 2015).

66 Below frequencies of 0.01 Hz and 0.1 Hz, the vertical and especially the horizontal components, are highly
 67 contaminated by tilt noise generated by ocean bottom currents (Webb, 1998; Crawford & Webb, 2000;
 68 Stähler et al., 2018, Fig. 1). The tilt noise level increases with signal period (see Fig. 1). The ocean bottom
 69 currents in many regions of the oceans are mostly driven by tidal force and often create a signal with
 70 strongest amplitudes below 1 Hz, appearing every 6–12 hours (e.g. Brink, 1995; Crawford & Webb, 2000;
 71 Ramakrushana Reddy et al., 2020; Essing et al., 2021). The ocean bottom currents passing the instrument
 72 create local eddy currents, deform the seafloor beneath the sensor and tilt the whole instrument frame, to
 73 which the seismometer is fixed (e.g. Duennebiele & Sutton, 1995; Webb, 1998; Romanowicz et al., 1998;
 74 Crawford & Webb, 2000; Corela, 2014; Stähler et al., 2018). Since the noise sources often act at
 75 frequencies of teleseismic earthquakes, it is crucial to improve the signal-to-noise ratio (SNR) on OBS
 76 recordings for the analysis of the Earth's crustal and mantle structure. Various studies discussed the
 77 improvement of OBS recordings through different approaches, either by suggesting a better OBS
 78 instrument design (Stähler et al., 2018, Corela, 2014, Essing et al., 2021), or by removing significant
 79 amounts of the noise from the contaminated data by signal processing (Crawford & Webb, 2000, Bell et al.,
 80 2015, Janiszewski et al., 2019). Our study follows the latter approach.

81 Crawford and Webb (2000) developed a method to remove noise from the vertical OBS component.
 82 Calculating the linear transfer function between the horizontal and the vertical component allows
 83 estimating the tilt noise which then can be subtracted from the vertical component. Pressure data measured
 84 in parallel to the seismometer recordings allow reducing the influence of infragravity waves on the vertical
 85 seismometer component recordings. For better results, Bell et al. (2015) propose to first rotate the
 86 horizontal components into the direction of the highest coherence between the horizontal and vertical
 87 component before calculating the linear transfer functions. The mentioned methods solely improve the
 88 SNR on the vertical component whereas the noise contamination on horizontal components is often larger.
 89 Other recent studies attempted to reduce noise also on the horizontal components (Mousavi and Langston,
 90 2017; Zhu et al., 2019; An et al., 2021; Negi et al., 2021). An et al. (2021) tried to reduce the noise on the
 91 horizontal components by applying the reversed procedure of Bell et al. (2015). Rotation of one horizontal
 92 component into the direction of the principle noise indeed results in an improvement of the orthogonal
 93 horizontal component, but the other horizontal component became noisier (An et al., 2021). Results of a
 94 recent study applying a polarization filter to reduce the noise on all components show strong changes of the
 95 broadband waveforms (Negi et al., 2021). The automatic noise-attenuation method developed by Mousavi
 96 and Langston (2017) is a time-frequency denoising algorithm using the wavelet transform and
 97 synchrosqueezing. It can be either used to keep the signal and remove the noise or vice versa. The
 98 decomposition method DeepDenoiser from Zhu et al. (2019) is based on a deep neural network.
 99 DeepDenoise decomposes the waveform into signal and noise in the time-frequency domain. The latter

Zahra Zali 10.1.2023 19:45

Deleted: If the seismometer mass is not perfectly leveled, the high tilt noise on the horizontal components is partially projected onto the vertical component (e.g. Crawford, 1994; Corela, 2014; Bell et al., 2015).

Zahra Zali 10.1.2023 13:43

Deleted: Hydrophone

106 methods, both improve the SNR, but mainly focus on local and regional earthquake detection. They result
107 in changes in the waveform shape if the noise amplitude directly ahead of the signal is significant in
108 comparison to the signal amplitude in a specific frequency. However, the analysis of undistorted broadband
109 waveforms on the horizontal components is crucial for many passive seismological structure analysis
110 methods, e.g. the calculation of receiver functions or surface wave dispersion and polarization analysis.

111 Here we introduce a method, inspired from ~~music information retrieval (MIR)~~ research, which is adapted to
112 seismological data and is used for noise reduction on both, the vertical and the horizontal components.

113 Seismic waveforms and acoustic signals generated by musical instruments are similar in some aspects
114 (Schlindwein et al., 1995; Johnson and Watson, 2019). The extensive research in the field of music
115 information retrieval has resulted in advances (e.g., Müller, 2015) that may be useful in seismic signal
116 processing as well. Exploiting the idea of harmonic-percussive separation (HPS) in MIR, Zali et al. (2021)
117 developed an algorithm to separate harmonic volcanic tremor from earthquakes in seismic waveforms. In
118 the present study we use this algorithm after some modifications in order to separate ‘harmonic’ (long-
119 lasting narrowband signals) and ‘percussive’ (broadband transients) components of an OBS data set aiming
120 at noise reduction and retrieval of clearer broadband earthquake waveforms. Throughout this study we will
121 make use of the term noise for any signal other than earthquake signal in the data set. In the context of OBS
122 noise reduction using HPS algorithms, percussive components correspond to earthquake signals and
123 harmonic components correspond to noise signals. The long-duration OBS noise signals that last a few
124 hours to days (depending on the noise type) with a restricted frequency range contrasts with transient
125 seismic signals such as earthquakes with a wider range of frequencies.

126 The algorithm introduced in Zali et al., (2021) is a combination of two HPS approaches that leads to the
127 desired signal separation. Here we also use the two approaches ~~in sequence~~ in order to separate different
128 type of noise signals from the earthquake signals. In the first step we ~~use~~ a similarity matrix (Rafii and
129 Pardo, 2012; Rafii et al., 2014) to separate monochromatic and harmonic noises. In the second step we ~~use~~
130 median filtering (FitzGerald, 2012) in order to separate the remaining narrow-band signals. With this two-
131 step approach we can separate and remove much of the OBS noise contamination from the earthquake
132 signals.

133

134 2 Data

135 In this study, we discuss the noise recorded by a LOBSTER (Longterm OBS for Tsunami and Earthquake
136 Research) OBS instrument from the DEPAS pool, which is equipped with a Guralp CMG-40T seismometer
137 ~~and~~ a MCS (Marine compact seismic) recorder ~~(for technical specification see Stähler et al., 2018)~~. We
138 show data recorded during the DOCTAR deployment, using DEPAS-LOBSTERS, located around the
139 Gloria Fault in the Northern Atlantic. Twelve DEPAS-LOBSTERS form the array. They were deployed
140 between 2011-2012 and recorded the data with a sampling frequency of 100 Hz (Hannemann et al., 2016;
141 Hannemann et al., 2017).

Zahra Zali 10.1.2023 20:08

Deleted: the

Zahra Zali 10.1.2023 14:05

Deleted: subsequently

Zahra Zali 10.1.2023 14:06

Deleted: adopt HPS using

Zahra Zali 10.1.2023 14:07

Deleted: adopt HPS using

Zahra Zali 11.1.2023 11:46

Deleted: and loose cables

Zahra Zali 10.1.2023 13:47

Deleted: Until 2019 the DEPAS LOBSTER OBS was built with an OBS-specific version of the Güralp CMG-40T/MCS recorder, where the seismometer had a corner frequency of 60 s and has been modified to last long on the seafloor (Stähler et al., 2018). However, the development of less power consumption lead to a higher noise level of the instrument itself (Stähler et al., 2018). At low frequencies (<0.1 Hz) the self-noise of the sensor is highly affecting the records, especially on the vertical component. However, the design of the DEPAS-LOBSTERS has been improved for deployments after 2019 (e.g. Essing et al., 2021).

Zahra Zali 10.1.2023 13:49

Deleted:

... [1]

We observed a continuous harmonic signal at a frequency of 0.04 Hz, partially with one or two overtones on a subset of the array (see Fig. 1). This signal was observed on 30% of the stations from the DOCTAR project (e.g., Hannemann et al, 2016, Hannemann et al., 2017) and on 43% of the stations from the KNIPAS project (Schlindwein et al., 2018), both using the mentioned DEPAS-LOBSTER design. We cannot identify the source of this signal yet, but based on its continuity, we assume an electronic source from the instrument itself.

The hydrophone and especially the horizontal components are highly affected by the strumming of the head-buoy, which is attached to the DEPAS-LOBSTER frame causing a ‘current-induced harmonic tremor signal’ (Stähler et al., 2018; Essing et al., 2021, Fig. 1). These ‘tremor events’ last over up to 4 hours and appear every 6–12 hours. These presumably tidal-driven tremor events are harmonic signals with a fundamental period of 0.4–1 s and various overtones (1–10 Hz) (Stähler et al., 2018; Essing et al., 2021, Fig. 1). Regarding the frequency band, ‘tremor events’ mainly affect the analysis of teleseismic body waves, especially on the horizontal component (Fig. 1).

3 Noise reduction methodology

3.1 Harmonic-percussive separation (HPS)

Harmonic-percussive separation refers to the problem of decomposing a signal into its harmonic and percussive components. This topic has received much attention in recent years (Rafii et al., 2018) and has numerous applications in the field of MIR and musical signal processing.

Within a general context harmonic signals show an overtone structure in the spectral domain. We call overtones one or more clear narrow-banded frequency peaks being integer multiples of the fundamental frequency (the first frequency peak in the spectrum). Harmonic signals have a relatively stable behavior over time and can be identified in a Short Time Fourier Transform (STFT) spectrogram by horizontal structures referred to constant frequencies along the time axis.

In contrast, percussive signals form vertical structures in a STFT spectrogram that contain energy in a wide range of frequencies. Therefore it is a straightforward strategy in most HPS algorithms to try to separate the horizontal structure from the vertical structure in the spectrogram corresponding to harmonic and percussive components, respectively. The horizontal lines in the spectrogram could correspond to either harmonic signals or monochromatic signals.

3.2 HPS using median filtering (MED)

199 | One of the simplest and fastest HPS approaches is median filtering (FitzGerald, 2010). For simplification
 200 | we name this algorithm as MED in this study. Median filters are usually used to remove noise from an
 201 | image or a signal. Using a median filter a sample will be replaced by the median of neighboring samples
 202 | within a window of a specific length (The specific length is the kernel size of the median filter). The entire
 203 | signal is processed using a sliding window analysis. Within the HPS, two median filters are applied to the
 204 | amplitude of the STFT spectrogram of a signal. One median filter is performed along the time axis of the
 205 | spectrogram to suppress percussive events and enhance harmonic components. Another median filter is
 206 | applied along the frequency axis in order to enhance percussive events and suppress harmonic components.
 207 | The two resulting spectrograms are then subsequently used to create two masks, which are applied to the
 208 | original signal spectrogram separately to generate two spectrograms of harmonic and percussive
 209 | components, respectively. For creating the harmonic and percussive signals in the time domain the phase of
 210 | the original signal is added to each spectrogram and the time domain signals are reconstructed using the
 211 | inverse STFT.

212

213 3.3 HPS using the similarity matrix (SIM)

214

215 | Another powerful approach in HPS proposed by Rafii & Pardo (2012) is based on calculating a similarity
 216 | matrix. We name this algorithm as SIM here. This approach is a repetition-based separation, which
 217 | identifies repeating elements in the spectrogram by looking for similarities by means of a similarity matrix.
 218 | Within the SIM algorithm, first similar time frames in the spectrogram are identified through a similarity
 219 | matrix. Then a median filter is applied only to the frames identified as similar to constitute the repeating
 220 | spectrogram model that corresponds to harmonic components. The non-repeating spectrogram that
 221 | corresponds to the percussive component of the data is obtained by subtracting the repeating spectrogram
 222 | from the original spectrogram. For creating repeating and nonrepeating signals in the time domain, the
 223 | phase of the original signal is added to each spectrogram and the time domain signals are reconstructed
 224 | using the inverse STFT. Details of this approach are discussed in the following section.

225

226 3.4 HPS noise reduction algorithm for OBS data

227

228 | The motivation for using HPS for noise reduction of OBS data stems from the different characteristic of
 229 | earthquake and OBS noise signals as described in section 2. Earthquakes are broadband transient signals,
 230 | while the signals of OBS noises are more narrow-band compared to earthquakes. We combine two
 231 | modified HPS algorithms to separate those signals in a two-step procedure. We divide the frequency
 232 | content of the signal into two frequency ranges; MED frequency range covers the frequency range between
 233 | 0.1 to 1 Hz whereas SIM frequency range contains the complementary frequency range, i.e. all frequencies
 234 | except the band between 0.1 and 1 Hz. Then two different algorithms are applied to these ranges,
 235 | respectively. In the first step, we use the SIM algorithm and separate only harmonic or monochromatic

Zahra Zali 10.1.2023 14:08

Deleted: In the context of

Zahra Zali 10.1.2023 14:08

Deleted: , one of the

Zahra Zali 10.1.2023 14:08

Deleted: simplest and fastest

Zahra Zali 10.1.2023 20:09

Deleted: the

Zahra Zali 10.1.2023 20:13

Deleted: S

Zahra Zali 10.1.2023 20:13

Deleted: .

Zahra Zali 11.1.2023 10:42

Deleted: range one

Zahra Zali 11.1.2023 10:43

Deleted: range two

Zahra Zali 11.1.2023 10:43

Deleted: range one and range two

245 signals from the original records in [the SIM frequency range](#). The reason is related to the frequency content
 246 of the noise and earthquake signals and how the SIM algorithm separates them. For a better understanding,
 247 we first explain how the algorithm works and then present more detail about this selection. In the second
 248 step, to reduce noise from [MED](#) frequency range we apply MED. There we target harmonic (or
 249 monochromatic) as well as narrow-band signals with gliding frequencies named as current-induced
 250 harmonic tremor signal in [section 2](#). The overall schematic diagram of our HPS noise reduction algorithm
 251 along with an example is shown in Fig. 2.

252 The SIM algorithm is explained in the following: From the original OBS record SO (SO represents the
 253 original restituted OBS signal) we derive the STFT named X being a complex-valued spectrogram.

254 The complex-valued spectrogram X is separated into its amplitude and phase components using Eq. 1.

255

$$X = V * \exp(1j * \varphi), \quad (1)$$

256

257 where φ is the phase of X , $V = |X|$ is the amplitude of X and j is the imaginary unit.

258 All of the spectrogram modifications will be applied to the amplitude spectrogram V . The cosine similarity
 259 (the similarity between two vectors of an inner product space) between the STFT time frames is calculated
 260 through the multiplication of the transposed V by V with the normalization of the V . This is shown in Eq. 2.

261

$$S(k_a, k_b) = \frac{\sum_{i=1}^n V(i, k_a) V(i, k_b)}{\sqrt{\sum_{i=1}^n V(i, k_a)^2} \sqrt{\sum_{i=1}^n V(i, k_b)^2}} \quad (2)$$

262

263 where S is the similarity matrix. Each point (k_a, k_b) in S is the cosine similarity between time frame k_a and
 264 k_b of V , $\forall k_{a,b} \in [1, m]$, where m is the number of time frames and n is the number of frequency channels
 265 for each time frame. Once the similarity matrix is calculated we use it to determine the most similar time
 266 frames to each single time frame. For time frame k_a we compare all the values in $S(k_a, k_l)$ for $l \in [1, m]$.
 267 We identify similar frames for time frame k_a , by choosing the upper 2% of the all time frames with the
 268 highest similarities.

269 Finally, all similar time frames to any frame k in V are stored in a temporary array K . Those similar time
 270 frames are used to create a repeating spectrogram model W . The corresponding frame in W is obtained by
 271 taking the median of K for each frequency at each time frame k . Those time-frequency bins, which are
 272 similar with little deviations between repeating frames, are captured by the median and constitute the
 273 repeating spectrogram model. This spectrogram contains only similar and repeating patterns. The time-
 274 frequency bins with large deviations between repeating frames would constitute nonrepeating transient
 275 patterns and would be suppressed by median filtering.

276

277 The nonnegative spectrogram V is the sum of two nonnegative spectrograms of repeating and nonrepeating

Zahra Zali 11.1.2023 10:47

Deleted: range two avoiding the frequency range of 0.1 to 1 Hz

Zahra Zali 11.1.2023 10:47

Deleted: the specified

Zahra Zali 10.1.2023 20:11

Deleted: the

Zahra Zali 10.1.2023 20:11

Deleted: S

Zahra Zali 10.1.2023 20:11

Deleted: .

patterns, hence, W (the repeating spectrogram model) should always have smaller values or at most be equal compared to V . To ensure this, a repeating spectrogram model \tilde{W} is defined by taking the minimum between W and V . The nonrepeating spectrogram model is derived by subtracting \tilde{W} from V .

We use these two (the repeating and the nonrepeating) spectrogram models to create two time-frequency masks for repeating and nonrepeating patterns, respectively. Instead of the binary mask, which is used in Rafii & Pardo (2012), we use soft mask via Wiener filtering (Vaseghi, 1996) which is more flexible and usually leads to a better result. The calculation of the soft masks is shown in the following equations:

$$M1 = \frac{\tilde{W}^2}{\tilde{W}^2 + (V - \tilde{W})^2}, \quad (3)$$

$$M2 = \frac{(V - \tilde{W})^2}{(V - \tilde{W})^2 + \tilde{W}^2}, \quad (4)$$

in which $M1$ and $M2$ are repeating and nonrepeating masks respectively. We multiply the masks with the input amplitude spectrogram V to separate the repeating and nonrepeating components. The element-wise multiplication of the masks by the input amplitude spectrogram V is shown in the following equations:

$$R = M1 \otimes V, \quad (5)$$

$$NR = M2 \otimes V, \quad (6)$$

in which R and NR denote repeating and nonrepeating amplitude spectrograms respectively.

The resulting R and NR spectrograms are shown in Fig. 2a for a specific/typical example of an OBS recording. As can be observed in the R spectrogram, in particular the low frequency harmonic or monochromatic signals below 0.1 Hz are well captured. We applied the SIM algorithm only to the frequency band below 0.1 Hz and above 1 Hz. In the frequency band from 0.1 Hz to 1 Hz the signals remain unchanged by this procedure. This is the first constraint we consider for the SIM algorithm. In the field of noise reduction using signal processing techniques, a very important point is to not modify the signals of interest for analysis. P and S waveforms in the teleseismic earthquake signals have often frequency content in the range of 0.1 Hz to 1 Hz with a dominant frequency around 0.3 Hz. Oceanic microseism noise, which is usually present in the OBS data, has a dominant frequency around 0.1 Hz to 0.3 Hz. As P and S phases have similar dominant frequency as the microseism noise wavefield, superposition

312 of both wavefields could happen in this frequency range. They could interfere constructively or
 313 destructively so the resulting amplitude could be higher or lower compared to the original P or S phase
 314 amplitudes. Considering these interferences, using the SIM algorithm, may result in creating fake higher
 315 amplitude for these phases or losing part of their amplitude in the noise reduced signal. But this could be
 316 problematic only when the amplitude of the noise is changing over the time. For a noise signal with almost
 317 constant amplitude, the SIM algorithm can extract the true amplitude of the noise even in the interference
 318 moments. However, the microseism noise has slightly varying amplitude over time.

319

320 Before moving to the second step we introduce a second constraint parameter, which we use in the SIM
 321 algorithm. Surface waves of teleseismic events show usually a dispersed narrow-band signal and
 322 correspond to mainly horizontal patterns of short duration (on a daily scale) in the spectrogram. Given the
 323 way the HPS separates harmonic from transient signals, the surface wavetrain may be erroneously
 324 recognized as harmonic component and thus be separated as noise signal. In order to prevent this and
 325 preserve the whole frequency content of the earthquake, we define a so-called waiting factor for the
 326 similarity calculation introducing a minimum time distance between two consecutive similar frames. For
 327 the problem of retaining teleseismic surface waves we found that a waiting factor of at least two hours
 328 prevents the algorithm to prune surface waves from the transient signal part. The rationale is that the
 329 duration of a teleseismic event is usually less than two hours whereas the noise components have longer
 330 duration. Using this waiting factor prevents separating any harmonic component of the earthquake signal as
 331 noise component. As a side effect this constraint causes that short-duration harmonic/monochromatic noise
 332 signals won't be well captured, too. However, these types of signals are not common in OBS data (see
 333 section 2).

334

335 In the second step of our algorithm, to target noise signals in the frequency range of 0.1 Hz to 1 Hz, we use
 336 MED as it is described in section 3.2. We apply this second part of the noise removal procedure only to a
 337 restricted frequency band of 0.1 Hz to 1 Hz. The dominant noise in the MED frequency range is the
 338 current-induced harmonic tremor signal (see section 2).

339 First we create the X' spectrogram which is equal to X in the MED frequency range and is equal to zero
 340 outside of this band. Then we apply a horizontal median filter to X' in order to separate harmonic
 341 components. This results in the harmonic spectrogram H , which contains near-horizontal patterns captured
 342 by the median filter.

343 Now we have two separated spectrograms for noise signals: R , which is derived from the first step, and H ,
 344 which is derived from the second step. Summing these two spectrograms will build the noise spectrogram
 345 N . Subtracting N from the input amplitude spectrogram V will construct the transient spectrogram T .

346 As can be seen in Fig. 2a in step 2, the dominant energy of the narrow-band signals with gliding
 347 frequencies in the range of 0.1 Hz to 1 Hz (the current-induced harmonic tremor noise as introduced in the
 348 section 2) is captured in the noise spectrogram N , but part of it remains in the transient spectrogram T .

Zahra Zali 10.1.2023 20:05

Deleted: is

Zahra Zali 10.1.2023 20:05

Deleted: ing

Zahra Zali 10.1.2023 14:11

Deleted: time

Zahra Zali 10.1.2023 20:12

Deleted: the

Zahra Zali 10.1.2023 20:12

Deleted: S

Zahra Zali 10.1.2023 20:12

Deleted: .

Zahra Zali 10.1.2023 20:13

Deleted: the

Zahra Zali 10.1.2023 20:13

Deleted: S

Zahra Zali 11.1.2023 10:50

Deleted: mentioned

Zahra Zali 10.1.2023 20:12

Deleted: the S

Zahra Zali 11.1.2023 10:50

Deleted: mentioned

Zahra Zali 10.1.2023 20:12

Deleted: S

Zahra Zali 10.1.2023 20:12

Deleted: .

Signals with changing frequency which don't form complete horizontal lines in the spectrogram, are difficult to capture by our HPS algorithm, so part of their energy remains in the final spectrogram.

3.5 Reconstruction of the denoised signal

In order to reconstruct the noise-removed signal in the time domain we must add phase information to the spectrogram. We had separated the complex-valued spectrogram X into its amplitude V and its phase component using Eq. 1 and all the further modifications have been applied to the amplitude spectrogram V . The phase of input signal SO is mostly affected by the phase of noise signals as they have the dominant energy in the signal. Therefore, we use the phase information of SO in order to reconstruct the noise signal. We add this phase to the noise spectrogram N using the following equation:

$$N' = N * \exp(1j * \varphi), \quad (7)$$

where N' is the complex-valued noise spectrogram. We reconstruct the noise signal NS from the complex spectrogram N' , using the inverse STFT. Finally the OBS denoised signal HPS (HPS here represents the SO signal after the HPS processing) is obtained by subtracting the noise signal from the input SO signal using the following equation:

$$HPS = SO - NS, \quad (8)$$

3.6 Parameters selection

Many typical noise signals observed in OBS recordings are harmonic, monochromatic or narrow-band signals with gliding frequencies (see [section 2](#)). In order to extract the expected narrowband noise signals from the STFT we require a high-frequency resolution in the spectral domain, therefore, making it necessary to use sufficiently long time windows for the spectral analysis. Here we use an FFT window length of 163.84 seconds with an overlap of 75%, corresponding to an FFT size of 16384 at a sampling frequency of 100 Hz, which corresponds to a frequency resolution of 0.006 Hz. We use a kernel size of 80 for the median filter in the MED algorithm. The larger the kernel size, the more noise signal would be captured. However, using very large sizes could introduce waveform distortions. As it is discussed in Driedger et al. (2021), the kernel size is not critical as far as not using extreme values. Our tests show that a kernel size of 80 is the largest size, which leads to a safe separation without capturing any energy of the teleseismic signal.

The values of parameters, which we used for this study, are presented in [Table 1](#). These are our recommendations for noise reduction of teleseismic earthquakes. One can tune the parameters based on

Zahra Zali 10.1.2023 20:12

Deleted: the

Zahra Zali 10.1.2023 20:12

Deleted: S

Zahra Zali 10.1.2023 20:12

Deleted: .

Zahra Zali 10.1.2023 20:14

Deleted: the

other specific applications such as denoising local earthquakes or extracting specific signals like microseism signal.

4 Results and Discussion

4.1 General Results

In this section we aim to demonstrate the reliability of our HPS noise reduction algorithm and evaluate the improvement of the OBS data. We applied the method to synthetic and real teleseismic earthquake data recorded by the OBS station D10 of the DOCTAR array (e.g., Hannemann et al, 2016, Hannemann et al., 2017). The synthetics were calculated for a source-receiver epicentral distance of 40° (focal depth: 45 km, focal mechanism: double couple, source duration: 4 s) by using the full wavefield software qseis (Wang, 1999) and a modified average ak135 velocity model including a water layer (Kennett et al, 1995). The crustal structure of the velocity model is adapted to the oceanic crust (crustal thickness is 6.6 km) in that area and the water depth is fixed to 4.9 km. Real oceanic noise of the ZRT components recorded by the station D10 is added to the corresponding components of the synthetic teleseismic signal. We created synthetics for three different noise situations at the beginning (N1), during (N2) and after (N3) tidal currents (Fig. 3) each with theoretical SNR of 1–10 between noise and P-onset on pure synthetic Z. Throughout the whole paper the SNR is defined as root mean square (RMS) of the signal divided by RMS of the noise. For further details of synthetic data creation see Fig. S2. For the comparison with real data, we selected in total 46 teleseismic events with magnitudes $M_w > 5.6$ and epicentral distances of $30\text{--}160^\circ$ (see Fig. S1). Here only those events were used, where a P onset could be visually identified. The pre-selection of the events is taken from Hannemann et al. (2017) and expanded by some events with low magnitudes (see Table S1). In the following, we will discuss the improvement of the records by comparing the seismograms and spectrograms of synthetic and real data. We also illustrate the improvement for two seismological applications (teleseismic surface wave group velocity analysis and receiver function analysis). For some observations, e.g. checking the phase arrival of the teleseismic body waves, we rotated the arbitrarily orientated horizontal components of the real data into the ZRT system. The orientation angles are taken from the previous study on the DOCTAR array (Hannemann et al., 2016).

Comparing the spectrograms and waveforms of the synthetic example we see a significant improvement of SNR in the HPS processed data set on all components (e.g. Fig. 3 and Fig. S3–5 for the real data). The continuous spectral lines of the assumed electronic noise are removed from the data, as well as most of the spectral lines related to tremor episodes of head-buoy strumming. During the tides, we observe a reduction of the spectral amplitudes for the tilt noise, as well as for the general background noise (Fig. 3 and Fig. S3–5) on the horizontal components. The results concluded from the spectrograms are confirmed by the spectra (Fig. 2b), which show the removal of the spectral peaks of the electronic noise (0.05, 0.1, 0.15 Hz) and the

436 | tremor episodes (0.5–1 Hz). The amplitude and phase information of the synthetic earthquake are preserved
437 | in the HPS signal (see Fig. 3).

438 | To quantify the improvements obtained when using our method, we calculated the cross-correlation of
439 | the teleseismic waveform, the SNR of the teleseismic body-wave phases and the RMS of the teleseismic
440 | waveform before and after denoising. Because most of the oceanic noise ranges at frequencies below 1 Hz,
441 | which is also the most interested frequency range of the OBS analysis, a 1 Hz low pass filter is applied to
442 | the signals before all result calculations.

443 | We calculated the correlation coefficient for synthetic SO and HPS compared with the synthetic earthquake
444 | signal for different SNR and noise realizations and plotted it in Fig. 4a. The high correlation coefficients for
445 | HPS and synthetic compared with SO and synthetic in all cases demonstrate a significant noise reduction.

446 | Furthermore, They indicate that the HPS denoising preserves the earthquake signal and doesn't introduce
447 | significant waveform distortions since the HPS is more similar to the synthetics compared to SO. In the
448 | following we show other measures that confirm the preservation of the earthquake signal.

449 | For the SNR calculation we used a signal window of 30 s starting from the theoretical onset (direct P on Z
450 | component, direct S on R and T component and Love wave on the T component) and a noise window of 60
451 | s starting 70 s before the theoretical onset. For the Love wave, the SV phase (R component) and P phase (Z
452 | component) the SNR increased significantly (Fig. 4b). We find that the noise type properties influence the
453 | perceived SNR improvement. It appears that there is no SNR improvement on the T-component for Noise
454 | situation N1 (Fig. 4b, the second panel). N1 is taken from the tidal current event's beginning, where there is
455 | a significant variation in noise-frequencies over time. In this instance, the signal and noise have comparable
456 | frequency ranges. Despite the SNR showing no increase, a visual check of the matching trace reveals a
457 | definite improvement in the waveform for the SH-wave on the T component. The results from the cross-
458 | correlation (Fig. 4a), confirm the improvement and preservation of the waveform. The SNR should not be
459 | utilized alone to assess the improvement by HPS noise reduction approach since we are concentrating on
460 | the preservation of the waveform and the SNR comparison strongly depends on the noise situation. The
461 | improvement of the traces by the HPS noise reduction approach is confirmed by the study of the cross-
462 | correlations, RMS (which is explained in the following paragraph), and the pure waveforms, even though
463 | the SNR is not improving in all instances.

464 | The RMS amplitudes of a noise-free R component synthetic, SO and HPS signals are estimated over 8
465 | seconds windows with 80% overlap and plotted in Fig. 4c. Comparing the RMS amplitude of the synthetic,
466 | SO and HPS we see that the synthetic and HPS have similar amplitude ranges while SO has a much higher
467 | amplitude. This shows a significant noise reduction in HPS along with preserving the energy of earthquake
468 | and all the phase arrivals. As there is some noise remaining after denoising we see some differences in the
469 | overall shapes of the RMS amplitude of the synthetic and HPS (especially after minute 24 which is almost
470 | at the end of the energy of the synthetic signal). However, HPS shows peaks on the arrival times of seismic
471 | phases of the synthetic which means that the energy of seismic phases is preserved after denoising. The
472 | minor changes in seismic phase shapes of the synthetic and HPS are also due to the remaining noise. The

Zahra Zali 10.1.2023 20:15

Deleted: whole

Zahra Zali 10.1.2023 20:15

Deleted: the

Zahra Zali 10.1.2023 20:07

Deleted: it is an indication

seismograms and spectrograms related to this example are presented in Fig. 3. Figure 4d shows a comparison of RMS amplitude of the original noise in SO (blue curve), the remaining noise in HPS after denoising (red curve) and the synthetic earthquake (green curve) signals. Besides a high noise reduction in HPS, the plot shows that the remaining noise is independent of the pattern of the synthetic earthquake, which confirms that the denoising process doesn't affect the earthquake energy in the HPS signal.

4.2 Applications

By applying our HPS noise reduction algorithm, we aim to improve seismological analyses, especially those involving the analysis of teleseismic body and surface waves. Valuable constraints of the Earth's structure in oceanic regions can be taken from the analysis of the SH-wavefield like Love-waves, which are not influenced by the water column, but often cannot be analyzed due to strong noise on the horizontal components. SV waves are also often masked by noise, but are for instance important for tomography studies or S and SKS shear wave splitting analysis (e.g. Silver and Chan, 1991). Other techniques using the SV-wavefield like the Z/R ratio of the teleseismic Rayleigh waves (Tanimoto & Rivera, 2008), or receiver functions (RF) (Langston, 1979) also rely on clear radial component readings. In the following we will show the improvement which was achieved for the SH arrivals and for the group velocity analysis of teleseismic Rayleigh- and Love waves, as well as for the receiver function analysis.

4.2.1 SH-waves

Since SH-waves are weak in energy and displayed on the noise-contaminated transversal horizontal component (T), they are sparsely observable on OBS recordings and are mostly masked by the high noise level. However, on the HPS processed data we see an improvement of the SNR on the T-component (see Fig. 4b). In many cases the SH-phase is clearly identifiable on the HPS T-component (see Fig. 3d for a synthetic data and Fig. S6 for a real data example).

4.2.2 Surface waves

Rayleigh waves in deep oceanic domains are strongly influenced by the water column, because most of the wave energy is traveling in the water. This poses a problem if the water depth changes along the travel path. Love waves are not influenced by the water column but are recorded only on horizontal components and their recordings on OBS systems are therefore more disturbed by strong noise sources like tilt-inducing tidal currents. To test the performance of the HPS noise reduction algorithm in the [low frequency](#) range, we performed a measurement of group velocities of Love and Rayleigh waves with the Multiple Filter Technique (MFT) (Dziewonski et al., 1969). Figure 5 shows group velocity curves for the synthetic Love wavetrain for the three noise situations N1-N3. For the MFT analysis we used the software mft96 (Herrmann, 2013). The unfiltered seismograms in the top panels (Fig. 5a-c) correspond to the P-wave SNR = 1 scenario. In all three cases the clarity of the dispersion curve is greatly enhanced in the images resulting from the HPS processed traces (Fig. 5e-g) in comparison to the noise free image (Fig. 5d). Also the

Zahra Zali 13.1.2023 12:19
Deleted: long period

seismogram traces improved greatly. The dispersion images show how noise energy is successfully removed from the frequency range of 0.05 to 0.2 Hz, which is the event frequency range. Lower frequency range which are weakly visible in the noise-free image (Fig. 5d) can not be recovered. The corresponding results for the Rayleigh wavetrain on the radial component are shown in Fig. S7. For the N3 case here also low frequency range down to 0.025 Hz can be successfully denoised.

For an evaluation of the HPS denoising technique on real surface wave data we selected 23 events with magnitudes larger than Mw 6.0 in the distance range between 47.5° and 159.6° and added one event with Mw= 5.6 at a distance of 37.9° (see Fig. S1). Figure S8 shows seismograms and MFT analysis examples for three events with different magnitudes and in different distances. The resulting group velocity dispersion curves for all 24 events for the original and processed data are shown in Fig. S9. For all components we find that the improved signal to noise ratio of the processed data allows the analysis of more events and of a broader frequency range than in the original data.

4.2.3 Receiver Functions

Receiver functions have been proven to be a valuable tool to observe the Earth's structure using teleseismic events (e.g., Langston, 1979, Ammon et al., 1995, Kind et al., 1995; Rondenay, 2009). Separating the source site from the receiver site by deconvolution allows to estimate the Earth's structure beneath the station. Here, we compare the receiver functions calculated from the synthetic examples and from real data before and after denoising (Fig. 6). The synthetics used for the receiver function calculation are pure synthetic signals contaminated by real noise (N1, N2, N3). On the synthetics, the SNR for P ranges between 1–10 (for detailed description of the synthetic creation, see section 4.1, Fig. 3 and S2). Receiver function analysis and the observation of the Earth's structure beneath the DOCTAR array was already calculated by Hannemann et al. (2017). Here, we don't aim to estimate the crustal and mantle structures, instead we aim to compare the P-receiver Functions of the radial component calculated from the original synthetic and real data (SO R-RF) with receiver functions of the radial component from the HPS processed synthetic and real data (HPS R-RF). To calculate the receiver functions, we applied the iterative deconvolution in the time domain (Ligorria & Ammon, 1999). We corrected the data for the Ps-phase, quality controlled (e.g. P-onset at 0 s on Z of HPS R-RF), stacked and low-pass filtered the synthetic data at 2 Hz and bandpass filtered the traces between 0.05–0.5 Hz for the real data with a zero-phase Butterworth filter. For both synthetic and real receiver function, the noise level strongly decreased and we observe a significant decrease in variance on the HPS traces compared to the SO traces (Fig. 6).

Our result shows that determination of the crustal- and mantle-phases is more reliable on the HPS R-RF stack than on the SO R-RF stack for both synthetic and real data (Fig. 6). We observe more distinct Ps-phase arrivals on the HPS R-RF than on the SO R-RF stack. The Ps-phases are caused by the P-to-S conversion at the Mohorovičić-, 410-km and 660-km discontinuity (hereafter referred to as Moho, 410, and 660, respectively; e.g. Deuss, 2009). For the synthetic example, we expect the P-to-s conversion at the Moho at depths of 11.5 km to arrive at 0.8s, which is better resolved in the synthetic HPS R-RF than in the synthetic SO R-RF, same for it's multiple (P_{MsPp}) and the water multiples every 6.5s (M_{WATER} , Fig. 6a).

Zahra Zali 10.1.2023 15:13

Deleted: map

Zahra Zali 10.1.2023 15:14

Deleted: that

Zahra Zali 10.1.2023 15:14

Deleted: also

Zahra Zali 10.1.2023 16:32

Deleted: in

Zahra Zali 10.1.2023 16:33

Deleted: range of the signal frequencies

Zahra Zali 10.1.2023 16:32

Deleted: is removed successfully

Zahra Zali 13.1.2023 12:16

Deleted: Longer signal periods

Zahra Zali 13.1.2023 12:17

Deleted: longer periods

Zahra Zali 13.1.2023 12:18

Deleted: 40

Zahra Zali 13.1.2023 12:18

Deleted: s

Zahra Zali 13.1.2023 12:18

Deleted: period

Zahra Zali 10.1.2023 20:13

Deleted: S

Zahra Zali 10.1.2023 20:13

Deleted: .

Assuming ak_{135} velocities we would expect the P_{410} -phase (Ps conversion at the 410) to arrive at around 43 s and the P_{660} -phase (Ps conversion at the 660) at around 66.8 s delayed to the direct P-arrival (see Fig. 6 a & b).

Instead of a rather weak peak on the SO-R-RF real data stack we observe a strong peak at around 43 s, with a good SNR on the HPS R-RF stack, indicating the sharp velocity contrast at the 410 (Fig. 6b). Comparing SO-RF and HPS-RF real data stacks, the amplitudes of the P_{660} -phase on the HPS decreased and became a broader peak. This aligns with our expectations from a conversion at a gradual velocity contrast as at the 660. These results are in line with the analysis of the crustal and mantle structure beneath the DOCTAR array presented by Hannemann et al. (2017). The negative phase (X1 in Fig. 6b) arriving at around 5 s is stronger on the HPS-R-RF real data stack than on the SO-R-RF real data stack and might either indicate the PpSs multiple of the Ps-phase at the Moho, or the direct P-to-s conversion at the LAB. On the HPS-R-RF real data stack we observe a strong positive phase (X2) arriving at 12 s (Fig. 6b). This phase has not been identified by Hannemann et al. (2017) and a detailed analysis of its origin is beyond the scope of this study, but it might be related to the water multiples.

5 Conclusions

In this work we have developed a method to separate the signals of teleseismic earthquakes from other signals in OBS recordings resulting in noise reduction of OBS data. Our method is a combination of two HPS algorithms from the field of [music information retrieval \(MIR\)](#) to separate harmonic and percussive components of OBS data. Earthquake signals as percussive components are separated from noise signals as harmonic components. The noise signal is reconstructed using the phase information of the original signal. Subtracting the noise signal from the original signal derives the noise-reduced signal. Our two-step HPS approach results in a cleaner, noise-reduced signal where the teleseismic broadband earthquake waveforms are preserved with their whole frequency content. Our synthetic tests shows that the SNR of HPS noise reduced signal significantly increases in most cases, however, the apparent SNR improvement depends on the noise type characteristics. The type of noise signals, which are eligible for our noise reduction algorithm contains most of the OBS noise energy.

The extracted noise signal contains some different signals where each can be derived by applying a band pass filter to the extracted noise signal in a proper frequency band. The derived signal may be used in researches related to that signal. For example the microseism signal can be extracted and used for investigation of the source generation area of microseisms.

From our analysis of the broadband seismograms, we find out that the improvement is significant and allows a broader and more reliable analysis of teleseismic earthquake data. Applications like the receiver function technique and SH-wave and Love wave analysis are considerably improved after applying the HPS noise reduction algorithm.

Group velocity analysis of teleseismic surface wavetrains showed that application of the HPS noise reduction technique allows to analyze more events and to analyze them in a broader frequency range. Especially more and wider Love wave dispersion curves could be recovered. The noise reduction algorithm improves the horizontal components significantly, which allows the OBS community to apply a broader range of seismological methodologies, including the horizontal components, to the OBS-data.

Code and data availability

A Python package named NoiseCut (Zali, 2022) and the code related to the proposed method along with an example of real data is freely available from <https://github.com/ZahraZali/NoiseCut>. The average computation time for this example (one day OBS signal with a sampling frequency of 100 Hz) is about 7 minutes on a PC with an Intel core i7 (six-core) processor of 2.2 GHz and 16 GB of RAM. A Jupyter notebook with all the Python codes and parameters related to the proposed method is available as an electronic supplement. The sea floor seismological data were archived by Alfred Wegener Institute (AWI), Helmholtz Centre for Polar Research, Bremerhaven, Germany, and are available upon request. The supplementary material related to this article contains list of all earthquakes used in this study and a map showing their location. The illustrations of the semi-synthetic data generation are presented in the supplementary material as well. An example of three components seismogram and spectrogram before and after applying HPS noise reduction algorithm to real data, Rayleigh wave group velocity analysis for a synthetic example, MFT analysis for three real events and group velocity curves for some real events are also presented through figures in the supplementary material.

Author contribution

Z.Z. developed the algorithm and designed the study. T.R. created the synthetics data, conducted the synthetic tests, and measured the receiver functions. F.K. conducted the group velocity analysis. Z.Z., T.R., and F.K. evaluated the results. Z.Z. and T.R. wrote the initial draft. All authors wrote the final manuscript and discussed the results.

Competing interests

The authors declare that they have no conflict of interest.

Acknowledgments

Zahra Zali is grateful for the support by the German Academic Exchange Service (DAAD) through the Graduate School Scholarship Programme under reference number 91721165. This work was also supported by the German Research Foundation (DFG MU 2686/13-1, SCHE 280/20-1) and the Daimler Benz Foundation (32-02/18). The sea floor seismological data were archived by Alfred Wegener Institute (AWI), Helmholtz Centre for Polar Research, Bremerhaven, Germany, and are available upon request. We acknowledge the DEutscher Geräte-Pool für Amphibische Seismologie (DEPAS) pool (Alfred-Wegener-

Zahra Zali 10.1.2023 15:40

Deleted: In conclusion, the presented method is a powerful algorithm for separation and extraction of different signals from OBS data and has especially application in noise reduction of OBS signals. -

Institut Helmholtz-Zentrum für Polar- und Meeresforschung et al., 2017) that is currently the largest European OBS pool. We acknowledge Sebastian Heimann for helping in packaging of the code related to the method. For building our method, we used Librosa, a Python package for audio and music signal processing (McFee et al., 2020). The data processing was done using obspy (Beyreuther et al., 2010) and pyrocko (Heimann et al., 2017); the receiver functions were calculated using the rf-package (Eulenfeld, 2020).

References

Alfred-Wegener-Institut, Helmholtz-Zentrum für Polar- und Meeresforschung et al.: DEPAS (Deutscher Geräte-Pool für amphibische Seismologie): German Instrument Pool for Amphibian Seismology, *J. Large-scale Res. Facil.*, 3, A122, <https://doi.org/10.17815/jlsrf-3-165>, 2017.

Ammon, C. J., Randall, G. E., & Zandt, G.: On the nonuniqueness of receiver function inversions, *J. Geophys. Res.-Sol. Ea.*, 95(B10), 15303-15318, <https://doi.org/10.1029/JB095iB10p15303>, 1990.

An, C., Cai, C., Zhou, L., & Yang, T.: Characteristics of Low-Frequency Horizontal Noise of Ocean-Bottom Seismic Data, *Seismol. Res. Lett.*, <https://doi.org/10.1785/0220200349>, 2021.

Bell, S. W., Forsyth, D. W., & Ruan, Y.: Removing noise from the vertical component records of ocean-bottom seismometers: Results from year one of the Cascadia Initiative, *B. Seismol. Soc. Am.*, 105(1), 300-313, <https://doi.org/10.1785/0120140054>, 2015.

Beyreuther, M., Barsch, R., Krischer, L., Megies, T., Behr, Y., Wassermann, J.: ObsPy: A Python Toolbox for Seismology, *Seismol. Res. Lett.*, 81(3), 530-533, 2010.

Brink, K. H.: Tidal and lower frequency currents above Fieberling Guyot, *J. Geophys. Res.-Oceans*, 100(C6), 10817-10832, <https://doi.org/10.1029/95JC00998>, 1995.

Corela, C.: Ocean bottom seismic noise: applications for the crust knowledge, interaction ocean-atmosphere and instrumental behaviour. Ph.D. thesis, University of Lisbon, 339 pp, 2014.

Crawford, W. C.: Determination of oceanic crustal shear velocity structure from seafloor compliance measurements (Doctoral dissertation, University of California, San Diego), 1994.

Crawford, W. C., & Webb, S. C.: Identifying and removing tilt noise from low-frequency (< 0.1 Hz) seafloor vertical seismic data, *B. Seismol. Soc. Am.*, 90(4), 952-963, <https://doi.org/10.1785/0119990121>, 2000.

678 Crawford, W. C., Webb, S. C., & Hildebrand, J. A.: Estimating shear velocities in the oceanic crust from
679 compliance measurements by two-dimensional finite difference modeling. *J. Geophys. Res.-Sol. Ea.*,
680 103(B5), 9895-9916, <https://doi.org/10.1029/97JB03532>, 1998.

681

682 Deuss, A.: Global observations of mantle discontinuities using SS and PP precursors. *Surv.*
683 *Geophys.*, 30(4-5), 301-326, <https://doi.org/10.1007/s10712-009-9078-y>, 2009.

684

685 Driedger, Jonathan, Meinard Müller, and Sascha Disch. "Extending Harmonic-Percussive Separation of
686 Audio Signals." In *ISMIR*, pp. 611-616. 2014.

687

688 Duennebieer, F. K., & Sutton, G. H.: Fidelity of ocean bottom seismic observations, *Oceanographic*
689 *Literature Review*, 10(43), 996, <https://doi.org/10.1007/BF01204343>, 1995.

690

691 Dziewonski, A., S. Bloch, and M. Landisman.: A technique for the analysis of transient seismic signals, *B.*
692 *Seismol. Soc. Am.*, 59, no. 1, 427-444, <https://doi.org/10.1785/BSSA0590010427>, 1969.

693

694 Essing, D., Schlindwein, V., Schmidt-Aursch, M. C., Hadziioannou, C., & Stähler, S. C.: Characteristics of
695 Current-Induced Harmonic Tremor Signals in Ocean-Bottom Seismometer Records, *Seismol. Res.*
696 *Let.*, 92(5), 3100-3112. , <https://doi.org/10.1785/0220200397>, 2021.

697

698 Eulenfeld, T.: rf: Receiver function calculation in seismology, *Journal of Open Source Software*, 5(48),
699 1808, <https://doi.org/10.21105/joss.01808>, 2020.

700

701 Fitzgerald, D.: Harmonic/percussive separation using median filtering, In *Proceedings of the International*
702 *Conference on Digital Audio Effects (DAFx)* (Vol. 13), 2010.

703

704 FitzGerald, D.: Vocal separation using nearest neighbours and median filtering, 23rd IET Irish Signals and
705 Systems Conference, Maynooth. 28-29th. June 2012, <https://doi.org/10.1049/ic.2012.0225>, 2012.

706

707 Friedrich, A., Krüger, F., & Klinge, K.: Ocean-generated microseismic noise located with the Gräfenberg
708 array, *J. Seismol.*, 2(1), 47-64, <https://doi.org/10.1023/A:1009788904007>, 1998.

709

710 Gaspà Rebull, O., Cusí, J. D., Ruiz Fernández, M., & Muset, J. G.: Tracking fin whale calls offshore the
711 Galicia Margin, north east Atlantic Ocean, *The Journal of the Acoustical Society of America*, 120(4), 2077-
712 2085, <https://doi.org/10.1121/1.2336751>, 2006.

713

714 Griffin, O. M.: Vortex-Induced Vibrations of Marine Cables and Structures, *NRL Memorandum Report*
715 5600, Naval Research Laboratory – Marine Technology Division, Washington D.C, 1985.

716
717 Hannemann, K., Krüger, F., Dahm, T., & Lange, D.: Structure of the oceanic lithosphere and upper mantle
718 north of the Gloria fault in the eastern mid-Atlantic by receiver function analysis, *J. Geophys. Res-Sol Ea.*,
719 122(10), 7927-7950, <https://doi.org/10.1002/2016JB013582>, 2017.
720
721 Hasselmann, K.: A statistical analysis of the generation of microseisms. *Rev. Geophys.*, 1(2), 177-210,
722 <https://doi.org/10.1029/RG001i002p00177>, 1963.
723
724 Heimann, S., Kriegerowski, M., Isken, M., Cesca, S., Daout, S., Grigoli, F., Juretzek, C., Megies, T.,
725 Nooshiri, N., Steinberg, A., Sudhaus, H., Vasyura-Bathke, H., Willey, T., Dahm, T.: Pyrocko - An open-
726 source seismology toolbox and library. V. 0.3. GFZ Data Services,
727 <https://doi.org/10.5880/GFZ.2.1.2017.001>, 2017.
728
729 Herrmann, R. B.: Computer programs in seismology: An evolving tool for instruction and research, *Seism.*
730 *Res. Lettr.*, 84, 1081-1088, <https://doi.org/10.1785/0220110096>, 2013.
731
732 Janiszewski, H. A., Gaherty, J. B., Abers, G. A., Gao, H., & Eilon, Z. C.: Amphibious surface-wave phase-
733 velocity measurements of the Cascadia subduction zone. *Geophys. J. Int.*, 217(3), 1929-1948,
734 <https://doi.org/10.1093/gji/ggz051>, 2019.
735
736 Johnson, J. B., & Watson, L. M.: Monitoring volcanic craters with infrasound “music”, *Eos*, 100.
737 <https://doi.org/10.1029/2019EO123979>, 2019.
738
739 Kennett, B. L., Engdahl, E. R., & Buland, R.: Constraints on seismic velocities in the Earth from
740 traveltimes. *Geophys. J. Int.*, 122(1), 108-124, <https://doi.org/10.1111/j.1365-246X.1995.tb03540.x>, 1995.
741
742 Kind, R., Kosarev, G. L., & Petersen, N. V.: Receiver functions at the stations of the German Regional
743 Seismic Network (GRSN). *Geophys. J. Int.*, 121(1), 191-202, <https://doi.org/10.1111/j.1365-246X.1995.tb03520.x>, 1995.
744
745
746 Langston, C.A.: Structure under Mount Rainier, Washington, inferred from teleseismic body waves. *J.*
747 *Geophys. Res.*, 84, 4749-4762, <https://doi.org/10.1029/JB084iB09p04749>, 1979.
748
749 Ligorria, J. P., & Ammon, C. J.: Iterative deconvolution and receiver-function estimation. *B. Seismol. Soc.*
750 *Am.*, 89(5), 1395-1400, <https://doi.org/10.1785/BSSA0890051395>, 1999.
751

752 Longuet-Higgins, M. S.: A theory of the origin of microseisms, *Philosophical Transactions of the Royal*
753 *Society of London. Series A, Mathematical and Physical Sciences*, 243(857), 1-35,
754 <https://doi.org/10.1098/rsta.1950.0012>, 1950.

755

756 McFee, B., V. Lostanlen, A. Metsai, M. McVicar, S. Balke, C. Thomé, C. Raffel, F. Zalkow, A. Malek,
757 Dana, et al.: *librosa/librosa: 0.8.0*, Version 0.8.0, Zenodo, <https://doi.org/10.5281/zenodo.3955228>, 2020.

758

759 Mousavi, S. M., & Langston, C.A.: Automatic noise-removal/signal-removal based on general cross-
760 validation thresholding in synchrosqueezed domain and its application on earthquake data. *Geophysics*,
761 82.4, V211-V227. <https://doi.org/10.1190/geo2016-0433.1>, 2017.

762

763 Müller, M.: *Fundamentals of music processing: Audio, analysis, algorithms, applications*. Cham,
764 Switzerland: Springer International Publishing. <https://doi.org/10.1007/978-3-319-21945-5>, 2015.

765

766 Negi, S. S., Kumar, A., Ningthoujam, L. S., & Pandey, D. K.: An Efficient Approach of Data Adaptive
767 Polarization Filter to Extract Teleseismic Phases from the Ocean-Bottom Seismograms. *Seismological*
768 *Society of America*, 92(1), 528-542, <https://doi.org/10.1785/0220200034>, 2021.

769

770 Olofsson, B.: Marine ambient seismic noise in the frequency range 1–10 Hz. *The Leading Edge*, 29(4),
771 418-435, <https://doi.org/10.1190/1.3378306>, 2010.

772

773 Pereira, A., Romagosa, M., Corela, C., Silva, M. A., & Matias, L.: Source Levels of 20 Hz Fin Whale
774 Notes Measured as Sound Pressure and Particle Velocity from Ocean-Bottom Seismometers in the North
775 Atlantic. *Journal of Marine Science and Engineering*, 9(6), 646, <https://doi.org/10.3390/jmse9060646>,
776 2021.

777

778 Pillet, R., Deschamps, A., Legrand, D., Virieux, J., Béthoux, N., & Yates, B.: Interpretation of broadband
779 ocean-bottom seismometer horizontal data seismic background noise, *B. Seismol. Soc. Am.*, 99(2B), 1333-
780 1342, <https://doi.org/10.1785/0120080123>, 2009.

781

782 Rafii, Z., Liutkus, A., & Pardo, B.: REPET for background/foreground separation in audio. In *Blind Source*
783 *Separation* (pp. 395-411). Springer, Berlin, Heidelberg, https://doi.org/10.1007/978-3-642-55016-4_14,
784 2014.

785

786 Rafii, Z., Liutkus, A., Stöter, F. R., Mimilakis, S. I., FitzGerald, D., & Pardo, B.: An overview of lead and
787 accompaniment separation in music, *IEEE/ACM Transactions on Audio, Speech, and Language*
788 *Processing*, 26(8), 1307-1335. <https://doi.org/10.1109/TASLP.2018.2825440>, 2018.

789
790 Rafii, Z., & Pardo, B.: Music/Voice Separation Using the Similarity Matrix, Proc. ISMIR, pp. 583-588,
791 2012.
792
793 Ramakrushana Reddy, T., Dewangan, P., Arya, L., Singha, P., & Kamesh Raju, K. A.: Tidal triggering of
794 the harmonic noise in ocean-bottom seismometers. *Seismol. Res. Lett.*, 91(2A), 803-813,
795 <https://doi.org/10.1785/0220190080>, 2020.
796
797 Rondenay, S.: Upper mantle imaging with array recordings of converted and scattered teleseismic waves.
798 *Surv. Geophys.*, 30(4), 377-405, <https://doi.org/10.1007/s10712-009-9071-5>, 2009.
799
800 Romanowicz, B., Stakes, D., Montagner, J. P., Tarits, P., Uhrhammer, R., Begnaud, M., Stutzmann, E.,
801 Pasyanos, M., Karczewski, J.F., Etchemendy, S. and Neuhauser, D.: MOISE: A pilot experiment towards
802 long term sea-floor geophysical observatories, *Earth, planets and space*, 50(11), 927-937,
803 <https://doi.org/10.1186/BF03352188>, 1998.
804
805 Schlindwein, V., Krüger, F., Schmidt-Aursch, M.: Project KNIPAS: DEPAS ocean-bottom seismometer
806 operations in the Greenland Sea in 2016-2017, Alfred Wegener Institute, Helmholtz Centre for Polar and
807 Marine Research, Bremerhaven, PANGAEA, <https://doi.org/10.1594/PANGAEA.896635>, 2018.
808
809 Schlindwein, V., Wassermann, J., & Scherbaum, F.: Spectral analysis of harmonic tremor signals at Mt.
810 Semeru volcano, Indonesia, *Geophys. Res. Lett.*, 22(13), 1685-1688. <https://doi.org/10.1029/95GL01433>,
811 1995.
812
813 Skop, R. A., & Griffin, O. M.: On a theory for the vortex-excited oscillations of flexible cylindrical
814 structures. *Journal of Sound and Vibration*, 41(3), 263-274, [https://doi.org/10.1016/S0022-460X\(75\)80173-](https://doi.org/10.1016/S0022-460X(75)80173-8)
815 8, 1975.
816
817 Silver, P.G. & Chan, W.W.: Shear wave splitting and subcontinental mantle deformation. *J. Geophys. Res.*,
818 96, 16429-16454, <https://doi.org/10.1029/91JB00899>, 1991.
819
820 Snodgrass, F. E., Hasselmann, K. F., Miller, G. R., Munk, W. H., & Powers, W. H.: Propagation of ocean
821 swell across the Pacific, *Philosophical Transactions of the Royal Society of London. Series A,*
822 *Mathematical and Physical Sciences*, 259(1103), 431-497, <https://doi.org/10.1098/rsta.1966.0022>, 1996.
823

824 Stähler, S. C., Schmidt-Aursch, M. C., Hein, G., & Mars, R.: A self-noise model for the German DEPAS
825 OBS pool. *Seismol. Res. Lett.*, 89(5), 1838-1845, <https://doi.org/10.1785/0220180056>, 2018.

826

827 Tanimoto, T., Rivera, L.: The ZH ratio method for long-period seismic data: sensitivity kernels and
828 observational techniques. *Geophys. J. Int.*, 172(1), 187-198, [https://doi.org/10.1111/j.1365-](https://doi.org/10.1111/j.1365-246X.2007.03609.x)
829 [246X.2007.03609.x](https://doi.org/10.1111/j.1365-246X.2007.03609.x), 2008.

830

831 Titze, I. R.: Nonlinear source-filter coupling in phonation: Theory, *The Journal of the Acoustical Society*
832 *of America*, 123(4), 1902-1915, <https://doi.org/10.1121/1.2832337>, 2008.

833

834 Vaseghi, S. V.: *Advanced signal processing and digital noise reduction*. Vieweg + Teubner Verlag,
835 <https://doi.org/10.1002/9780470740156>, 1996.

836

837 Wang, R.: A simple orthonormalization method for stable and efficient computation of Green's
838 functions, *B. Seismol. Soc. Am.*, 89(3), 733-741, <https://doi.org/10.1785/BSSA0890030733>, 1999.

839

840 Webb, S. C.: Broadband seismology and noise under the ocean, *Rev. Geophys.*, 36(1), 105-142,
841 <https://doi.org/10.1029/97RG02287>, 1998.

842

843 Webb, S. C., Zhang, X., & Crawford, W.: Infragravity waves in the deep ocean, *J. Geophys. Res.-*
844 *Oceans*, 96(C2), 2723-2736, <https://doi.org/10.1029/90JC02212>, 1991.

845

846 Zahra Zali. (2022). *ZahraZali/NoiseCut: NoiseCut (v1.0.0)*. Zenodo.
847 <https://doi.org/10.5281/zenodo.7339552>

848

849 Zali, Z., Ohrnberger, M., Scherbaum, F., Cotton, F., & Eibl, E. P.: Volcanic Tremor Extraction and
850 Earthquake Detection Using Music Information Retrieval Algorithms, *Seismol. Res. Lett.*, 92(6), 3668-
851 3681, <https://doi.org/10.1785/0220210016>, 2021.

852

853 Zhu, W., Mousavi, S. M., & Beroza, G. C.: Seismic signal denoising and decomposition using deep neural
854 networks. *IEEE T. Geosci. Remote.*, 57(11), 9476-9488. <https://doi.org/10.1109/TGRS.2019.2926772>,
855 2019.

856

857

858

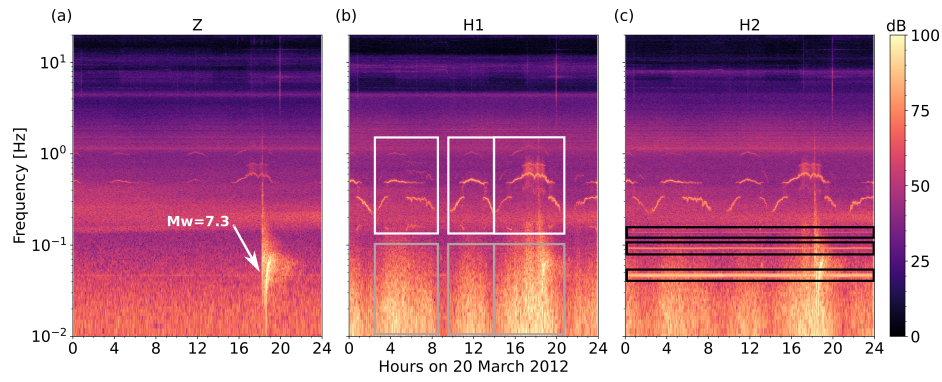
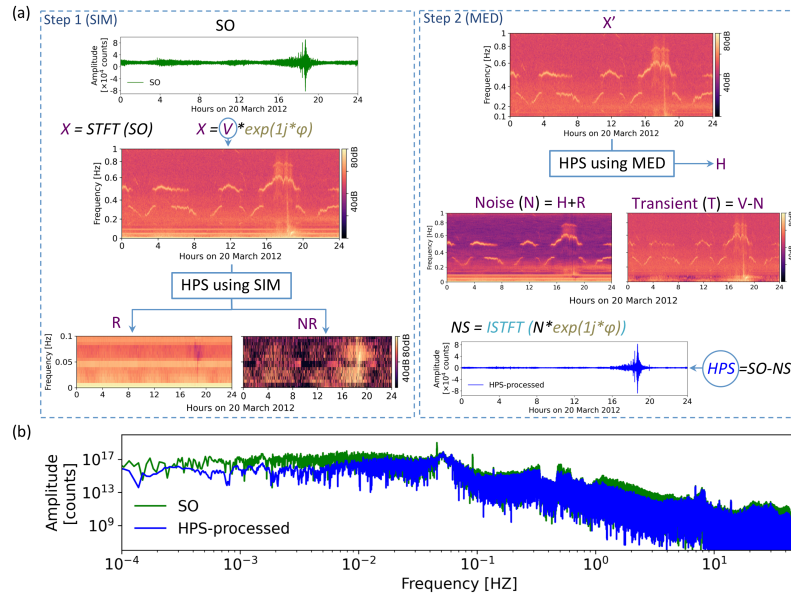


Figure 1: Spectrogram of an one-day OBS signal shows ocean bottom noise on Z (a), H1 (b) and H2 (c) components. The data was recorded by the station D10 of the DOCTAR array with a sampling frequency of 100 Hz. The spectrogram were calculated using a window length of 2^{16} sample and an overlap of 75%. The signal of an earthquake (Mw=7.3) on 20.3.2012 at around 18:00 at the station D10 is shown in (a). The tidal cycle of the current-induced noise is clearly visible during the high tilt noise episodes (gray box in b). The white box in (b) highlights the tremor episodes caused by the head buoy strumming. On H2 (c) we see an instrument-related, presumably electronic noise (black boxes). The high energy of the secondary microseism band at around 0.2 Hz is visible on all components.

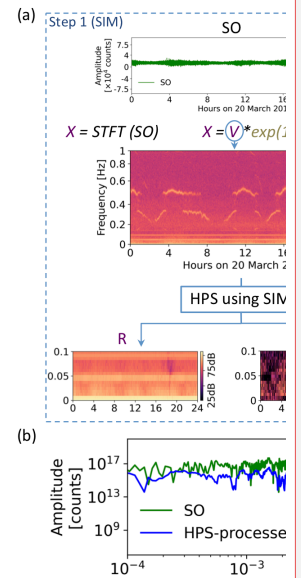
869
870



871
872
873
874
875
876
877
878
879
880
881
882
883
884
885
886

Figure 2: Method flowchart (a) Illustration of the processing steps with a real data example. Left panel shows the first step of the method where using the similarity matrix (SIM) in the frequency range below 0.1 Hz and above 1 Hz, we divide the spectrogram (X) of the original signal (SO) into two spectrograms of repeating (R) and non-repeating (NR) patterns. Right panel shows the second step of the method where we apply a median filter (MED) to the frequency range of 0.1 to 1 Hz (spectrogram X') in order to remove noises from this frequency range. It results in the harmonic spectrogram (H). As the interested frequency range for OBS signals is below 1 Hz, the spectrograms show only this frequency range. Finally the noise spectrogram (N) is created by summing the separated noises derived from two steps and the noise signal (NS) is derived using ISTFT. We obtain the noise reduced signal (HPS) by subtracting the NS from the input OBS signal (SO). STFT, short time Fourier transform. HPS, harmonic-percussive separation. SIM, similarity matrix. MED, median filtering. ISTFT, Inverse Short Time Fourier Transform. (b) Spectrum of the original signal (SO) and the HPS noise reduced signal.

Zahra Zali 11.1.2023 14:22



Deleted:

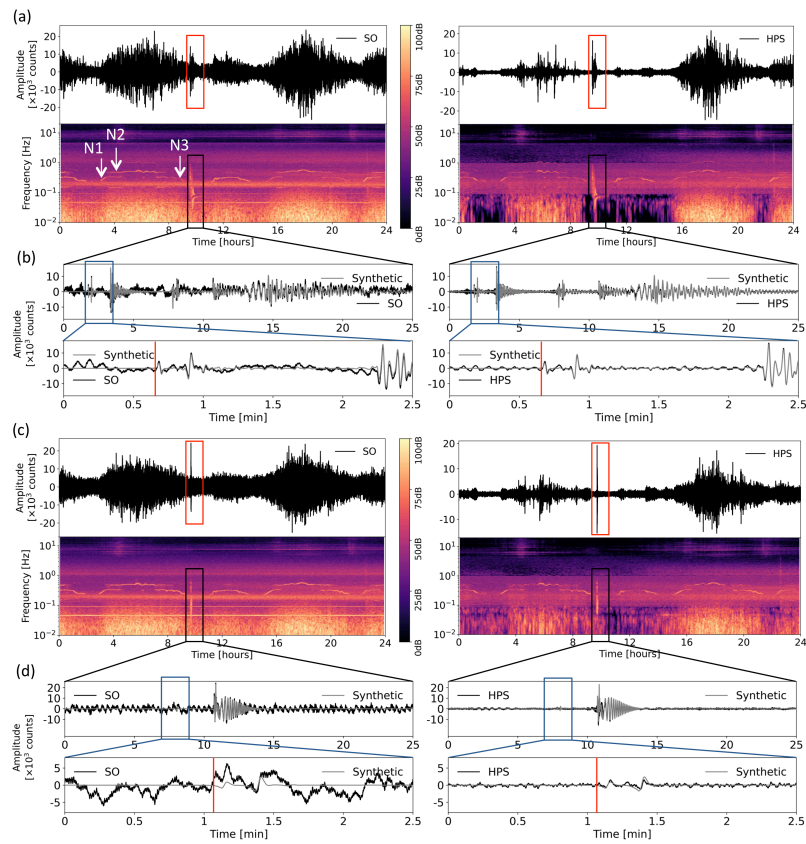


Figure 3: Comparison of the synthetic seismograms and spectrograms of the original signal SO and the HPS noise reduced signal on the R and T components for a synthetic signal with SNR= 1.5 before denoising. (a) & (c) Show one day seismograms and spectrograms for R and T components, respectively. Squares show the earthquake section. The arrows in (a) show three noise situations (N1-N3). (b) & (d) Show seismograms of the earthquake section on SO and HPS signals, with detailed view of the P-arrival (on component R in subfigure b) and SH-arrival (on component T in subfigure d). Red lines show P-arrivals in (b) and SH-arrival in (d).

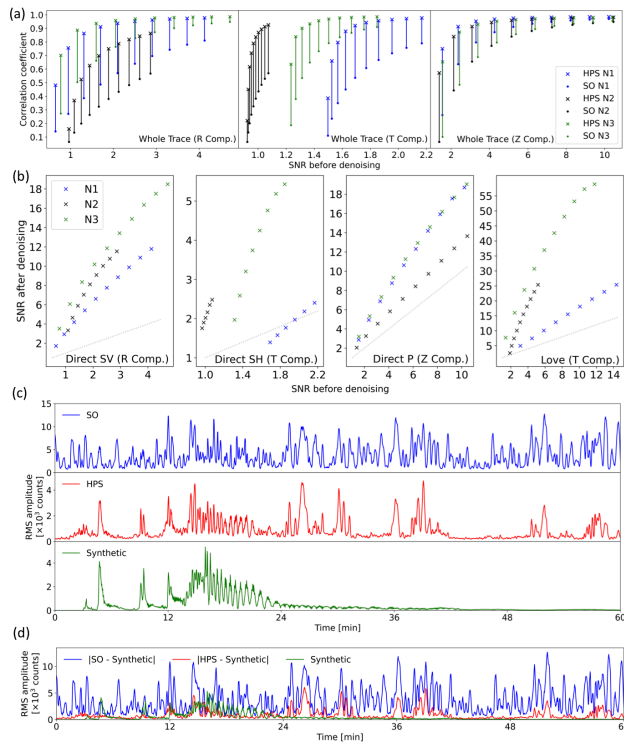
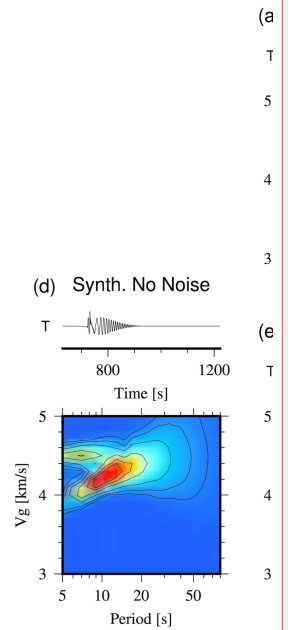


Figure 4: Comparison of the synthetic SO and HPS signals (both are lowpass filtered at 1Hz). (a) Correlation coefficients (for the whole trace) for different SNRs and 3 realistic noise realizations for Z, R and T components (Component is abbreviated as Comp.). (b) Improvement of SNR for direct body wave phases and the Love wave. The gray dotted lines in (b) mark the line with gradient 1 (no improvement of SNR). (c) Comparison of the root mean square (RMS) amplitude of one example of the SO, HPS and synthetic earthquake signals. This signal is the same example shown in Fig. 3 (R component, SNR= 1.5 before denoising). (d) The RMS of the original noise (blue trace: |SO - Synthetic|) and the remained noise after denoising (red trace: |HPS- Synthetic|) compared to the synthetic earthquake signal.

Zahra Zali 13.1.2023 12:13



Deleted:

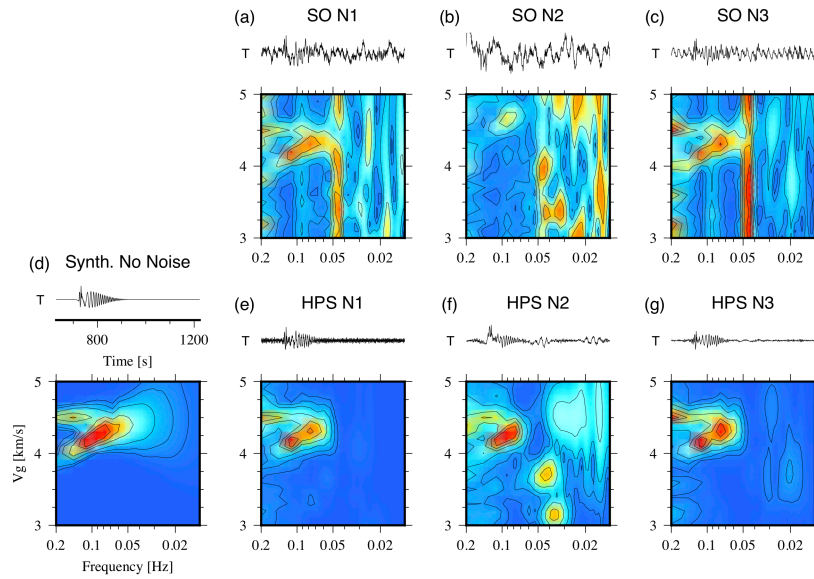


Figure 5: Love wave group velocity analysis for unfiltered and HPS processed synthetic Love wavetrains contaminated by three real world OBS noise signals (noise situations N1-N3, station D10, DOCTAR experiment, see [section 2](#) for more details). (a)–(c): Lower panels: Unfiltered synthetic signal (SO) MFT analysis results. Top panels: seismogram time windows corresponding to the range of group velocities shown on the y-axis. (d) Noise free synthetic case. (e)–(g): HPS processed input traces for noise situations N1-N3 (lower panel: MFT analysis result, top panel: HPS processed seismogram).

Zahra Zali 10.1.2023 20:13

Deleted: S

Zahra Zali 10.1.2023 20:13

Deleted: .

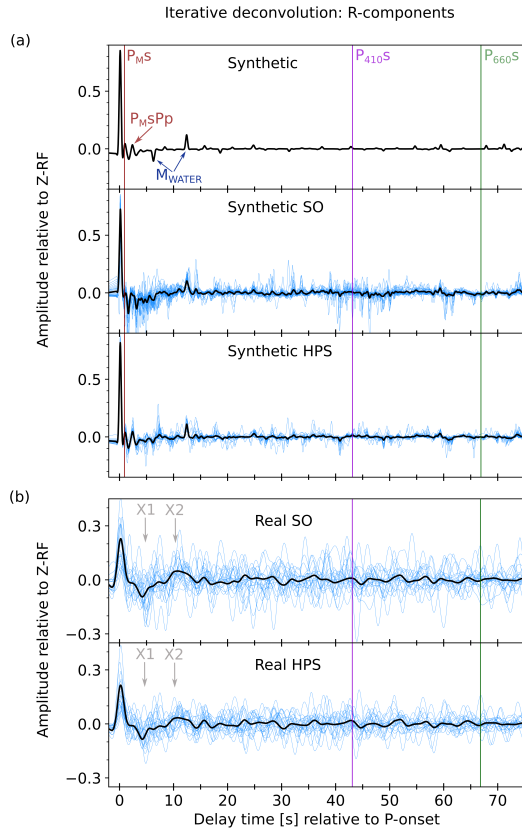


Figure 6: R-receiver function comparison of synthetic and real data examples. (a) Comparison of the synthetic data examples, lowpass filtered at 2 Hz. The pure synthetic R-RF is shown in the uppermost panel, followed by the synthetic SO and the synthetic HPS R-RFs. The black lines show the summed individual R-RFs (blue waveforms). The theoretical onset times for this specific model are marked. Red line: Ps-arrival of the Moho (P_{Ms}) and its multiple (P_{MsPp}), violet line: Ps arrival of the 410 (P_{410s}), green line: Ps-arrival of the 660 (P_{660s}), dark-blue arrows: Multiples in the watercolumn of 4.9 km (M_{WATER}), repetitive every 6.5s. (b) Comparison of the real data, bandpass filtered at 0.05–0.5 Hz. The upper panel shows the R-RFs of the real SO traces and the lowermost panel the R-RFs of the real HPS traces. The individual traces (blue) are shown as stack (black line) and the theoretical onset times based on the average ak135 velocity model are shown as violet line (P_{410s}) and green line (P_{660s}). The origin of the phases X1 and X2 (gray) remain unclarified, since their interpretation is beyond the scope of this study.

930 **Table 1: Parameters values used in our study**

Parameters	FFT window size	FFT overlapping percentage	SIM frequency range	SIM waiting factor	SIM upper threshold	MED frequency range	MED kernel size
Values	16384 samples	75%	[0-0.1] & above 1 Hz	2 hours	2%	[0.1-1] Hz	80

931

Zahra Zali 10.1.2023 14:34
Deleted: Frequency range for

Zahra Zali 10.1.2023 14:34
Deleted: Frequency range for

Zahra Zali 10.1.2023 15:43
Deleted: in MED